UC Irvine
UC Irvine Previously Published Works

Understanding the Role of Interfaces for Water Management in Platinum Group Metal-Free Electrodes in Polymer Electrolyte Fuel Cells

Jiangjin Liu,[†,‡] Morteza Rezaei Talarposhti,[‡,§] Tristan Asset,[‡,§] Dinesh C. Sabarirajan,[†] Dilworth Y. Parkinson,[‖] Plamen Atanassov,[‡,§] and Iryna V. Zenyuk*[‡,§]
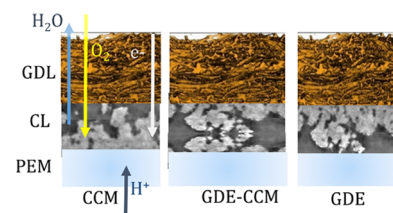
[†]Department of Mechanical Engineering, Tufts University, Medford, Massachusetts 02155, United States

[‡]National Fuel Cell Research Center, University of California, Irvine, California 92697, United States

[§]Department of Chemical and Biomolecular Engineering, University of California, Irvine, California 92697, United States

[‖]Advanced Light Source, Lawrence Berkeley National Laboratory, Berkeley, California 94720, United States

ABSTRACT: A systematic analysis, both experimental and model-assisted, has been performed over three main configurations of platinum group metal-free (PGM-free) electrodes in polymer electrolyte fuel cells (PEFCs): catalyst-coated membrane CCM technology is being compared to the gas-diffusion electrode (GDE) method of electrode fabrication and juxtaposed to a hybrid/combined GDE-CCM method of membrane-electrode assembly (MEA) fabrication. The corresponding electrodes were evaluated for their electrochemical performance, modeled, and studied with in situ and *operando* X-ray computed tomography (X-ray CT). The study establishes that through-thickness inhomogeneities play the most important role in water withdrawal/water management and affect most significantly PGM-free PEFC performance. The catalyst integration technique results in formation of interfacial regions with increased porosity and surface roughness. These regions form critical interfaces de facto responsible for flooding type behavior of the PEFC as shown for a first time by *operando* X-ray CT. The computational model shows that the PEFC performance critically depends on liquid water formation and transport at cold and wet conditions.

1. INTRODUCTION

Polymer electrolyte fuel cells (PEFCs) are a promising clean energy conversion technology to replace the internal combustion engine due to their high efficiency and power density.[1] Platinum catalyst cost can compose up to 40% of the total cost of the fuel cell stack,[2] which sets a barrier for the mass commercialization of fuel cell vehicles (FCVs). To reduce the cost, there is a need for either substantial reduction of Pt loading in the cathode catalyst layer[3,4] or use platinum group metal-free (PGM-free) electrocatalysts.[5] Atomically dispersed Fe−N−C electrocatalyst is the emerging advanced type of PGM-free catalyst, its activity arising from a multitude of actives sites, e.g., atomically dispersed iron in nitrogen coordination (FeN_x), along with pyridinic and pyrrolic nitrogen moieties in graphene structures, often viewed as cocatalytic (bifunctional sites).[6,7] While the exact contribution of each type of active sites to the oxygen reduction reaction (ORR) mechanism and pathway is still being debated, an emerging consensus is that there is a strong codependence between chemical makeup of the active site and morphological features at which it has been displayed. In recent years, significant progresses have been achieved to increase the activity and durability of the PGM-free electrocatalysts for oxygen reduction reaction (ORR).[8−23] Yet the challenges remain to reach the Department of Energy (DOE) target activity of 44 mA/cm^{2} at 0.9 V. Among many challenges is the role water plays in the overall ORR process and whether or not the reaction can become product-release dependent and thus additional "water overpotential" can arise even in the region of catalytic control. This is even more important when PGM-free catalysts are being incorporated in membrane-electrode assemblies (MEA) as cathode catalyst layers. In these triphase interpenetrated porous layers, water is not only a chemical ORR product but also undergoes capillary condensation as a liquid phase. The resulting phenomenon is known as "electrode flooding", and it is associated with blocking gas pathways for oxygen supply and water withdrawal, resulting in increased overpotentials.

Despite substantial advances over the past decade of intensive development, PGM-free electrodes have lower volumetric activity comparing to the traditional Pt-based electrodes due to either lower turnover-frequency and/or

lower number of active sites. To compensate for lower volumetric activity, PGM-free electrodes use a higher loading of ~4 mg/cm^2 (as usually the catalyst cost factors are not significant), resulting in order of magnitude thicker electrodes (~100 μm) compared to conventional Pt/C electrodes. This larger thickness can result in overall mass transport and Ohmic losses.[5,24,25] Most current studies focus on increasing the activity of PGM-free electrocatalyst toward ORR, hence resulting in little discussion on the electrode morphology,[24,26−31] while systematic studies of PGM-free catalyst layers' robustness at different temperatures and relative humidity are practically absent in archival literature.

Several studies focused on understanding mass transport in PGM-free electrodes of the polymer electrolyte fuel cells (PEFC). Pavlicek et al.[29] expanded the method developed by Reshetenko et al.[32] to dilute oxygen with nitrogen, argon, and helium to determine the gas-phase and nongas-phase resistances.[29] They observed higher mass-transport resistances for PGM-free electrodes compared to conventional Pt/C electrocatalysts and used a pseudo two-dimensional model, which includes composition changes along the flow channel, to explain the trends. Komini Babu et al.[27] observed the ionic limitations induced by the PGM-free electrodes, along with local flooding. Serov[33] et al. have shown that PGM-free electrodes exhibit a highly inhomogeneous through thickness structure, with substantially broad distribution of catalysts agglomerates. This inhomogeneity results in electrodes with a high tortuosity value of 5, which can be detrimental for both ionic and gas-phase transport. Therefore, it is critical to understand morphology of the fully integrated, state-of-the-art catalyst layer and the resulting interfaces. In our previous work,[28] we have demonstrated water accumulation in large voids at the interface between membrane and catalyst layer. This was mainly due to electrode fabrication method, where gas diffusion electrode (GDE) is formed by depositing catalyst ink onto the microporous layer (MPL) of gas diffusion layer (GDL) before this being hot-pressed onto the polymer electrolyte membrane resulting in complete MEA.

Depending on the fabrication process, the MEA in PEFC can be classified into two types: based on GDE and catalyst coated membrane (CCM) fabrication. CCM method includes deposition of the electrocatalyst ink onto the membrane before hot-pressing onto the GDL. In general, when practicing CCM assembly, care must be taken, as PGM-free catalyst layers are thick (~100 μm) and evaporative drying results in an inhomogeneous surface and sometimes in a network of interconnected "mud-cracks".[34] The two MEA fabrication methods can be combined or hybridized, i.e., half (or an aliquot) of the electrocatalyst ink is deposited on the membrane and another half (or residual portion) on the GDL, before hot-pressing, to yield a composite GDE-CCM electrode. This method sometimes is termed as a double-layered cathode in the PGM community, where either catalyst loading[35] or ionomer distribution[36] is varied in this configuration for improved catalyst utilization, improved interfacial contact to limit water pooling. Figure 1 shows a schematic of hypothesized/envisioned interfaces for the PGM-free electrodes in the CCM, GDE, and GDE-CCM configuration. Electrode's bulk morphology, as well as the character of the interfacial regions will dictate mass-transport and water distribution in these types of PGM-free electrodes.

Imaging techniques are powerful tools to study morphology and transport processes within operating PEFCs.[37] Focused
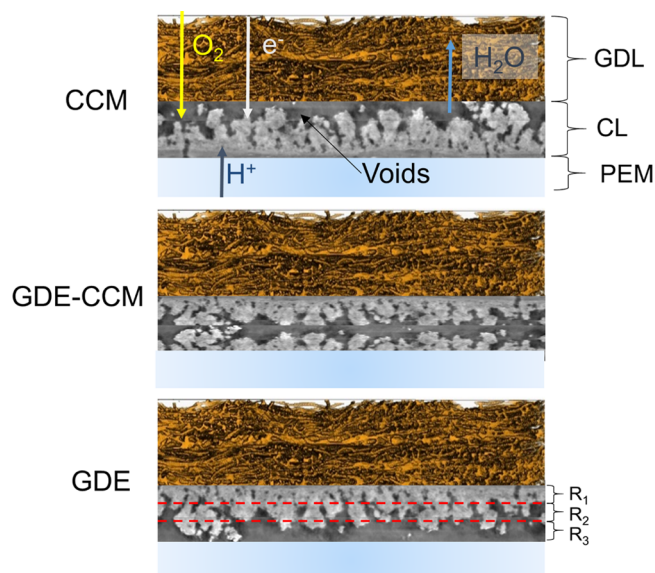

Figure 1. Three types of fabricated electrodes: CCM, GDE-CCM, and GDE. The resulting interfaces are represented schematically.

ion beam-scanning electron microscopy (FIB-SEM)[31] and nano X-ray computed tomography (CT),[26,38] which have high resolutions of tens of nanometers, were applied to study the microstructure within the PGM-free electrodes. The full thickness of the electrode and its interfaces with membrane or GDL cannot be easily resolved with these techniques due to their limited field of view (FOV). Neutron radiography,[39] which can be used as an *operando* technique with a large FOV, can be applied to study the water distribution in the electrodes. It is a two-dimensional technique, and its resolution (~10 μm) does not allow the imaging of the finer details of the agglomerates within the PGM-free electrodes (desirably felling within 1 μm range). Micro X-ray CT, which has a resolution of ~1 μm and FOV of 3.2−4 mm, is well suited for elucidating the morphological structure of the larger macrospores and agglomerates.[33]

In our previous study, we used a combination of the *operando* micro X-ray CT and *ex-situ* nano X-ray CT to directly visualize water formation and transport at the nano- and microscales in the PGM-free electrodes.[28] We have shown that significant water pooling occurs at the interface between the GDE and membrane because the electrode was highly hydrophobic. This water pooling was reduced at higher operating temperatures due to evaporative water removal. Furthermore, water distribution tracked closely with the porosity of the electrode.

In this study, we extend the *operando* X-ray CT analysis to systematically investigate the three types of PGM-free electrodes: GDE, CCM, and GDE-CCM. The polarization curves under different temperatures are experimentally measured and numerically calculated. Electrochemical characterizations, i.e., polarization curve, open-circuit voltage (OCV), and high-frequency resistance (HFR), are conducted at the synchrotron beamline along with image collections. First, an *in situ* study is conducted to confirm the hydrophobic nature of the GDE and to measure water evaporation rates to gain insight into the flooding phenomena. Then, water distributions within the three types of PGM-free electrodes are visualized by *operando* X-ray CT. A continuum cross-sectional multiphase model is applied to study the PGM-free electrodes perform-
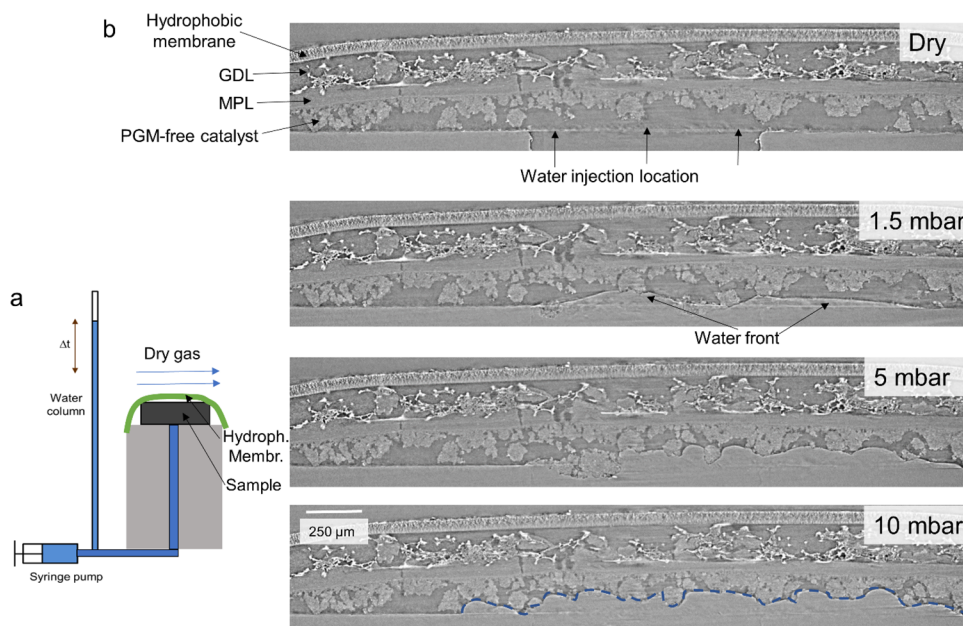
Figure 2. (a) Schematic of the experimental setup for water injection and evaporation measurements and (b) cross-section tomographs of water-injection into the GDE at 1.5, 5, and 10 mbar of liquid water pressure.

ance under varied saturation levels. The influence of the electrode interfacial region on local current density, Ohmic losses, and mass transport resistance are analyzed.

2. MATERIALS AND CATALYST SYNTHESIS PROTOCOL

The PGM-free ORR catalyst in this study was of the transition metal−nitrogen−carbon (M−N−C) type. The nitrogen-doped carbonaceous material with atomically dispersed iron was synthesized as following. A calculated amount of a mix of silica (i.e., homemade Stöber spheres, LM-150 and OX-50-Cab-O-Sil) were combined with $Fe(NO_3)_3$ 0.9 H_2O and an aromatic amine charge-transfer organic salt, nicarbazin (Sigma-Aldrich). The reactants were mixed with distilled water to form a homogeneous, viscous solution which was dried overnight at 45 °C under continuous stirring. The material was then dried over a second night before being ground and ball-milled. A pyrolysis at 975 °C under 7% H_2−93% N_2 then followed for 45 min. This pyrolysis consisted of insertion of the catalyst at 525 °C and temperature ramp to 900 °C in 12 min (31.25 °C/min). Then an increase of temperature to 975 °C followed for 8 min (9.375 °C/min). The materials were then leached during 4 days in a 2:1 HF−HNO_3 mixture, before being washed until reaching neutral pH. The catalysts were then dried, ball-milled, and pyrolyzed for 30 min at 950 °C. For this pyrolysis, the catalyst was inserted when the furnace reached 950 °C. Final ball-milling followed the second pyrolysis. All the ball-milling was performed for 30 min at 45 Hz.

The CCM, GDE, and GDE-CCM were sprayed all by hand using air compressor spray guns on a hot plate at 60 °C (the spraying was done on the membrane (Nafion Membrane XL) for the CCM, GDL (SIGRACEL GDE BC29) for the GDE, and equally divided between the membrane and the GDL. The target loadings were 4 mg/cm^2 for the nonprecious metal catalyst on CCM and GDE (for the GDE-CCM the sprayed loading was equally divided between the two surfaces). The inks were composed of catalyst, isopropyl alcohol and 5% wt Nafion. The latter loading was measured to be 45%. The ink

was sonicated for 20 min before deposition. The geometrical area of the MEAs was 5 cm^2. They were assembled by hot-pressing the GDE on the membrane for the GDE, the CCM on the GDL for the CCM , and the GDE and the CCM for the GDE-CCM at 120 °C and 450 psi for 10 min. Subgasket thickness on the anode side of the fuel cell was 150 μm and 250 μm for the cathode side.

3. EXPERIMENTAL PROCEDURES

3.1. X-ray Computed Tomography. Micro X-ray CT was performed at the Advanced Light Source (ALS) at Lawrence Berkeley National Laboratory (LBNL), Beamline 8.3.2. X-ray energy of 24 keV was selected with a double-multilayer monochromator. The optical detection system consisted of a 0.5 mm LuAG scintillator and 5× lenses with a sCMOS PCO Edge camera, resulting in a 1.3 μm pixel size. The horizontal FOV was 3.3 mm. For each CT scan, 1025 projections were collected over a 180 deg rotation, using a 300 ms exposure time. Three FOVs were collected for each operating cell to observe a full active area along the channels.

For water injection and evaporation experiments, the details for the experimental setup have been reported in our previous study.[40] Here we summarize the approach and setup. Figure 2a shows a schematic of the experimental setup. A GDE was sandwiched between the injection plate and hydrophobic membrane on the top in such a way that the GDE was facing the injection plate. Water was injected through a 3.2 mm aluminum injection plate, and water pressure was controlled by setting the height of the water column. Nitrogen flowed parallel and on the top of the hydrophobic membrane at a flow-rate of 200 mL/min to set zero relative humidity conditions on the top. The timer was set, and over the period of 0.5 mm decrease in the water column, after which the time was recorded and X-ray CT scan was performed. The liquid water pressure was set to 1.5, 5, and 10 mbar.

A prior version of the *operando* fuel cell hardware design and its location at the beamline was reported in our earlier study.[28] Briefly, the cell consists of graphite bipolar plates with two parallel 1 mm × 1 mm channels machined into them. The active area of the *operando* cell is about 2 cm × 0.5 cm. The imaging area did not consist of any aluminum enclosure, whereas the top and bottom of the cell was clamped with aluminum plates to ensure sufficient compression. Hard-stop gaskets were used to reach 20% cell compression. Two

Table 1. Model Dimensions, Phases Present, and Porosity

	M	aCL	cCL	MPL	GDL	CH	L	Plate
thickness (μm)	18	2	90	40	180	500	500	500
phases present, α	M	s, G, L, M	s, G, L, M	s, G, L	s, G, L	G	s	s
porosity, ϵ	0	0.65	0.55~0.8	0.4	0.8	1	0	0

cartridge heaters and thermocouples were used to control the temperature of the cell.

3.2. Image Processing and Visualization. TomoPy was used to retrieve the phase and to perform tomographic reconstructions. The Gridrec algorithm within TomoPy was used for tomographic reconstructions. Our earlier work[33] reports more details on reconstruction parameters. ImageJ and Avizo were used for image segmentation, analysis, and visualization.

3.3. Electrochemical Characterization. The membrane electrode assemblies (MEAs) were loaded into a fuel cell test station (Fuel Cell Technologies). The graphite flow plates had a single serpentine pattern. Testing parameters were to flood the cells at three different temperatures, i.e., 35 °C, 45 °C, and at 80 °C, with 100% relative humidity (RH) where there was 250 sccm hydrogen at the anode and 200 sccm air at the cathode at a back pressure of 20 psi both for the anode and cathode. Fuel cell testing was performed and the data was collected at the potential ranges between 0.2 to 1.1 V with 60 s potential holds. The polarization curves and the power density data were acquired at the end of each cycle.

4. MODEL DESCRIPTION

The model is developed by Balliet and Newman[41,42] and modified by Zenyuk et al.[43] Here we provide only salient details. It is a two-dimensional cross-section PEFC model. The modeling domain includes membrane (PEM), anode and cathode catalyst layers (CL), microporous layers (MPL), gas diffusion layers (GDL), channels (CH) and lands (L), and plates (Plate). The model domain dimensions are summarized in Table 1. s, G, L, and M denote solid, gas, liquid, and membrane phases, respectively. Porosity values for GDL were directly obtained by micro X-ray CT image segmentation and also confirmed with our previous study;[44] porosity values for the bulk of the cCL were previously obtained by us with nano X-ray CT and interfacial values are obtained via segmenting images in this study and also are confirmed from our previous study.[33] The value for MPL was adopted by thresholding data from ref 45.

Here, we just present general physics, boundary conditions, and modifications of the model to be applied for PGM-free catalyst layers. The cathode catalyst layer was divided into three regions (as shown in Figure 1), i.e., R1, R2, R3. Each region has a thickness of 30 μm. As a result of the fabrication process, each type of electrode (i.e., CCM, GDE, GDE-CCM) presents a region with a larger porosity and lower ionomer volume fraction regions. For example, the region R3 of the CCM has a porosity of 0.8 and an ionomer volume fraction of 0.1, whereas its regions R1 and R2 have a porosity of 0.55 and an ionomer volume fraction of 0.21. These large porosity, lower volume fraction region correspond to the interfacial region of the electrode, i.e., where the electrode was hot-pressed: (i) between the catalyst layer and the GDL for the CCM, (ii) between the catalyst layer and the membrane for the GDE, and (iii) in the middle of the catalytic layer for the GDE-CCM.

Liquid and Gas Transport. Darcy's law and conservation of mass are applied to study the liquid and gas transport.

$$N_\alpha = -\frac{\rho_\alpha \kappa_\alpha^{\text{eff}}}{\mu_\alpha} \nabla P_\alpha \tag{1}$$

$$\nabla \cdot (N_\alpha) = s_v + s_{\text{rxn}} \tag{2}$$

where ρ is the density, κ^{eff} is the effective permeability, μ is the viscosity, and P is the pressure. Subscript α specifies the liquid phase or gas phase. s_v is phase change source term, and s_{rxn} is reaction source term. Gas pressure is specified as the operating PEFC pressure at the CH|GDL interface. If $P_L < P_G + P_c$, the no-flux boundary condition is set, otherwise $P_L = P_G + P_c$ is set at the CH|GDL interface. P_L, P_G, and P_c are the liquid, gas, and capillary pressures, respectively.

Gas Diffusion. The Stefan−Maxwell equation is used to study the gas diffusion.

$$\nabla \cdot \left(-\rho_G \omega_i \sum_j^n \bar{D}_{ij}^{\text{eff}} (\nabla x_j + (x_j - w_j)\nabla P_G / P_G) \right) + \rho_G (v \cdot \nabla)\omega_i$$
$$= s_{v,\omega_i} + s_{\text{rxn},\omega_i} \tag{3}$$

where ω_j and x_j are the mass and molar fractions of species j, respectively. v is the velocity vector. $\bar{D}_{ij}^{\text{eff}}$ is the effective diffusion coefficient, and it accounts for the porosity and tortuosity factor of the material. Thermal diffusion is neglected.

$$\bar{D}_{ij}^{\text{eff}} = \frac{\epsilon_G}{\tau_G} \frac{p\bar{D}_{ij}}{P_G} \tag{4}$$

where ϵ_G is the volume fraction of the gas phase, and τ_G is the tortuosity of the gas phase. The binary diffusion coefficient $p\bar{D}_{ij}$ depends on the gas mixture composition.[46] The reactant volume fraction and relative humidity (RH) are specified at the CH|GDL interface.

Electron Transport. Electronic current is calculated as

$$i_1 = -\sigma^{\text{eff}} \nabla \phi_1 \tag{5}$$

σ^{eff} is the effective electronic conductivity, and ϕ_1 is the electronic potential. The conservation of electronic charge is considered:

$$\nabla \cdot i_1 = -i_h^{\text{rxn}} \tag{6}$$

The local current density is calculated by the kinetics described in detail by Zenyuk et al.[43] The electronic potential is set as the cell potential at the outside boundary of the cathode bipolar plate. The zero potential is set at the outside boundary of the anode bipolar plate.

Ion Transport. Weber and Newman's membrane model is modified to include water transport in the liquid and vapor phases.[47,48] Ionic current is calculated as

$$i_2 = -\left[(1 - S)\left(\kappa_V \nabla \phi_2 + \frac{\kappa_V \xi_V}{F} \nabla \mu_w \right) \right.$$
$$\left. + S\left(\kappa_L \nabla \phi_2 + \frac{\kappa_L \xi_L}{F} \nabla \mu_w \right) \right] \tag{7}$$
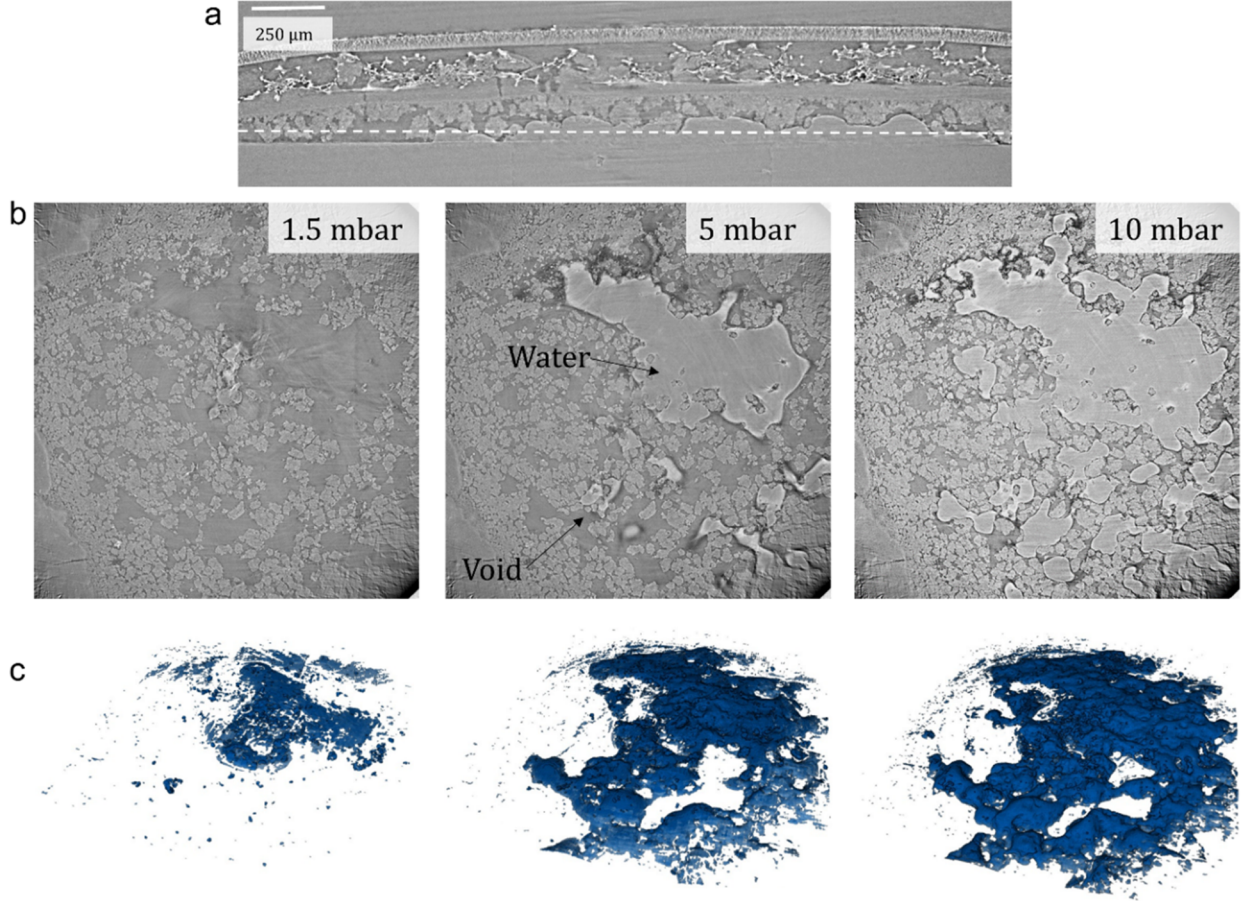
Figure 3. (a) Through-plane cross-section with a dashed line, for which the in-plane cross-section are shown; (b) in-plane cross sections of the GDE with liquid water at 1.5, 5, and 10 mbar of pressure; and (c) volume-rendering water distribution for 1.5, 5, and 10 mbar of water pressure.

where S is the liquid water saturation in the ionomer phase, κ is the ionic conductivity, ξ is the electroosmotic coefficient, and μ_w is the chemical potential of water in the ionomer phase. Water flux in the membrane is calculated as

$$\mathbf{N}_w = -\left[(1-S)\left(\frac{\kappa_V\xi_V M_w}{F}\nabla\phi_2 + M_w\left(\alpha_V + \frac{\kappa_V\xi_V{}^2}{F^2}\right)\nabla\mu_w\right)\right.$$
$$\left. + S\left(\frac{\kappa_L\xi_L M_w}{F}\nabla\phi_2 + M_w\left(\alpha_L + \frac{\kappa_L\xi_L{}^2}{F^2}\right)\nabla\mu_w\right)\right] \tag{8}$$

The conservation of ions and water are considered:

$$\nabla\cdot\mathbf{i}_2 = -i_h^{\mathrm{rxn}} \tag{9}$$

$$\nabla\cdot\mathbf{N}_w = -R_{v,\mathrm{M}} \tag{10}$$

The no-flux boundary conditions are set at the CL|GDL interface.

Heat Transfer. Thermal equilibrium is assumed between different phases. The conservation of energy is applied to calculate the temperature (T) distribution:

$$\sum_\alpha \epsilon_\alpha\rho_\alpha\hat{C}_{p,\alpha}\left(\frac{\partial T}{\partial t} + \mathbf{v}_\alpha\cdot\nabla T\right) - k^{\mathrm{eff}}\nabla\cdot(\nabla T)$$
$$= Q_v + Q_{\mathrm{jle}} + Q_{\mathrm{rxn}} \tag{11}$$

where $\hat{C}_{p,\alpha}$ is the specific heat, k^{eff} is the effective thermal conductivity. Q_v, Q_{jle}, and Q_{rxn} are the heat source terms of phase change, joule heating and heat of reaction, respectively. A constant cell temperature, i.e., 40 °C, is set at the outside of the bipolar plate in this study.

Capillary Pressure and Saturation. The capillary pressure is defined by the Young−Laplace equation:

$$p_c = \frac{2\gamma}{r} \tag{12}$$

where γ is the surface tension and r is the pore radius. Liquid water fills larger pores first since the electrodes are hydrophobic. As Figure S1[33] in the Supporting Information shows, water saturation is quite different in different regions of the cathode at each capillary pressure. The interfacial region, which has much larger pore radii than the others will be flooded first. In the model, we calculate the water saturation as an interpolation function of capillary pressure according to the data from the water retention curves. To account for the different pore sizes in different regions, the water retention curves of Q3 and Q1 have been implemented to the porous region and other two regions, respectively. The residual saturation is set as 0.3.

5. RESULTS

5.1. *In Situ* X-ray CT Water Injection. Figure 2 shows cross-section tomographs of the PGM-free GDE for dry and three liquid water pressures (1.5, 5, and 10 mbar). Water injection experiments were performed to simulate water distribution within the GDE during the PEFC operation,
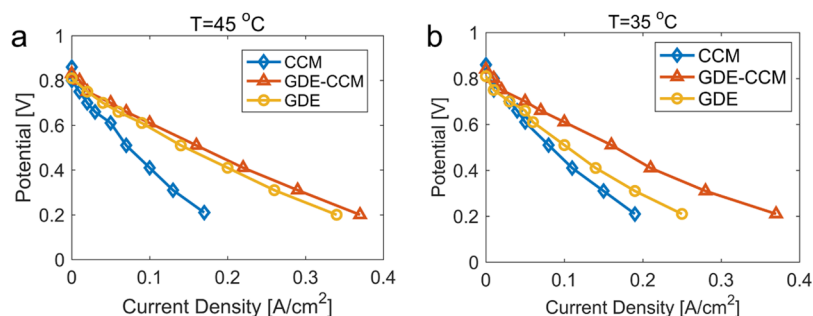
Figure 4. Polarization curves for three types of electrodes for (a) 45 °C and (b) 35 °C. The testing conditions were flow-rate 250/200 sccm, no back-pressure, humidifier temperatures 50/50 °C.
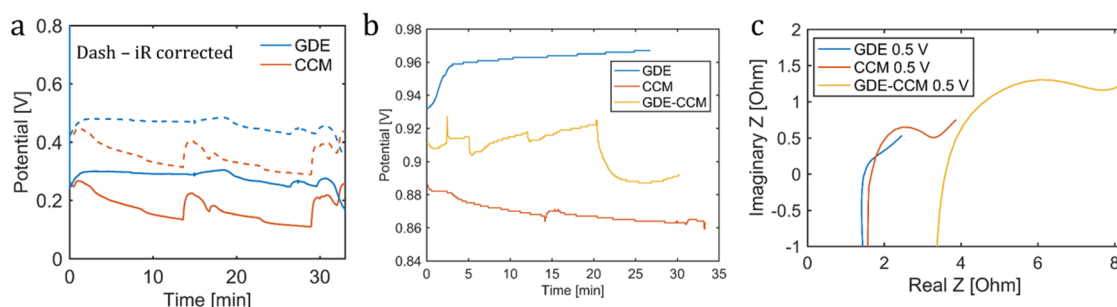

Figure 5. Electrochemical data collected at the beamline: (a) potentials at constant current holds for GDE and CCM cells at 100 mA/cm^2, the testing conditions were 35 °C cell, humidifier temperatures 40/40 °C, 100/200 sccm, no back-pressure; (b) OCV for three electrodes; and (c) HFR for three electrodes.

essentially assessing the GDL's wettabilty. We previously reported water imbibition studies into the GDLs,[49] coupled to the study of evaporation rates.[40] Typically, water breakthrough (condition when liquid water passes through the layer and emerges at the other side) is reached at 5 mbar water pressure for GDLs without MPLs, whereas when the MPL is present, which is highly hydrophobic, the water breakthrough pressure is 1 order of magnitude higher. With Figure 2, we observe that the water front forms a continuous layer between the GDE and the injection plate. At 5 mbar, it spreads laterally, as there is a gap due to the inhomogeneous electrode structure. At 10 mbar, water is present in large voids, but it is almost nonwetting when it comes in contact with the catalyst.

Figure 3 shows water distribution in the in-plane view and 3D volume-rendering. As already mentioned at 1.5 mbar, water has not yet filled many of the voids, whereas at 5 mbar water is present in all the large voids and at 10 mbar it starts to fill smaller gaps within the electrode. It still does not wet the electrode completely, and by the shape of the water clusters, one can clearly see that the catalyst is highly hydrophobic, this being confirmed by a previous study[28] showing a contact of 150° for this catalyst. 3D volume-renderings show the shape of water clusters, indicating hemispherical shapes of nonwetting nature, as previously observed in the *operando* study.[28] Nafion is hydrophilic; therefore, the injection plate—GDE interface here simulates that of the interface with Nafion.

We simultaneously collected evaporation rates for given liquid water pressures. These evaporation rates are per projected area (3.2 mm diameter circle) and are not normalized by the surface area of the water front. We have previously shown that, at 30 °C, water evaporation rates within GDLs are diffusion-limited and scale with surface area of water front available for evaporation.[40] Here, we observe an increase in evaporation rate with the increase of the liquid water

pressure, induced by (i) its increase of surface area, as more water is injected, and (ii) the decrease of its diffusion length, as the water front is advancing. These results are shown in the Supporting Information.

5.2. Polarization Curves. Figure 4 shows polarization curves for three electrode configurations at two temperatures: 45 and 35 °C. At 45 °C, the GDE and GDE-CCM showed similar polarization behavior, with GDE-CCM showing slightly higher current densities. The CCM had lower performance, about half of the current density at 0.2 V compared to the other two cases. Reducing the temperature further to 35 °C results in similar polarization curves for GDE-CCM and CCM compared to 45 °C but reduced current densities for GDE. At 0.2 V, the current density decreased from 0.35 A/cm^2 at 45 °C to 0.25 A/cm^2 at 35 °C. This performance drop is quite interesting, as we expect water content in the cell not to change significantly between 35 and 45 °C. The onset potential for current density decrease is ~0.7 V, which leads us to believe that the cell experiences proton-transport limitations. The GDE configuration has the least contact points with the membrane and, as later discussed in the modeling section, is prone to ionic limitations. Figure S2a in the Supporting Information shows the polarization curves for GDE, CCM, and GDE-CCM at 80 °C. For a given GDE, similar performance was obtained at Tufts and UNM. No back-pressure was applied for the experiment. Both GDE and GDE-CCM had very similar polarization curves at 80 °C; however, CCM showed worse polarization behavior. Up until 0.6 V, all GDEs, CCM, and GDE-CCM had very similar current densities; however, as potential decreased below 0.6 V, the current density for the CCM became lower than current density for GDE and GDE-CCM. CCM is fabricated by direct deposition of ink onto a membrane. The drying behavior of ink deposited onto a membrane is very different from that deposited onto
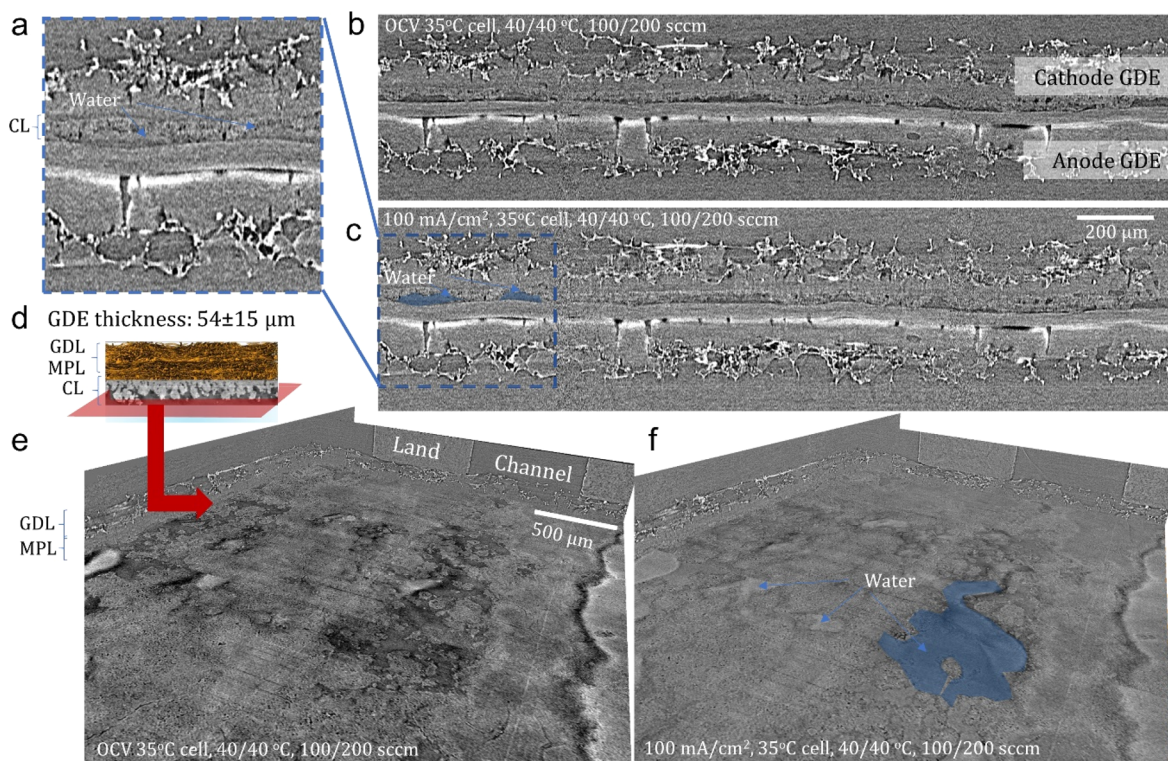
Figure 6. *Operando* X-ray CT cross sections for the cell with the GDE. The comparison of the cross sections under the channel (with part (a) the zoom-in) between the cell operating at (b) OCV and (c) 100 mA/cm². In-plane view (with part (d) the location) of the CL|PEM interface at (e) OCV and (f) 100 mA/cm². Selected locations of interfacial water accumulation are shown with false coloring.

MPL.[50] As will be shown later in the CCM configuration, the layer is more uniform, less porous, and thicker than in the GDE configuration, and these morphological properties will have additional impact on polarization behavior. At 0.2 V, all the electrodes have higher current densities at 80 °C compared to 45 and 35 °C, which indicates the mass transport limitations are more significant at low temperatures. Figure S2b in the Supporting Information shows model results for the low-potential region superimposed over the experimental results to show the model calibration study.

Figure 5a shows potentials recorded at constant current density holds of 100 mA/cm² during the *operando* synchrotron X-ray CT scans for CCM and GDE cells. The potential for the GDE cell was higher than for the CCM cell, consistent with the laboratory polarization curves. Average potential during the 30 min hold for GDE was 0.28 V, whereas for the CCM it was 0.17 V, and this amounts to a 0.11 V difference. Comparing this difference to the laboratory polarization curves at 100 mA/cm² and 35 °C (Figure 4b), we can see that the difference is also approximately 0.1 V. The *iR* corrected potential plots are also shown in Figure 5a, where the average values are similar to those obtained during the polarization curve measurements in the laboratory. Note that the CCM potential profile from Figure 5a shows periodic increases in potential, and these are due to a physical cell moving in and out of the line of X-rays, straining the current carrying copper wire and improving contact resistances between the wire and graphite hardware. Figure S2c shows the polarization curve for the CCM obtained at the beamline, where the current densities are compatible to those obtained in conventional hardware in the laboratory setting (Figure 4).

The OCVs for the GDE, CCM, and GDE-CCM electrodes are reported in Figure 5b. The GDE had the highest OCV at around 0.96 V, and the GDE-CCM had the second highest value of 0.88−0.90 V and the CCM had the lowest OCV value of 0.86−0.88 V. The Nyquist plot at 0.5 V is shown for the three electrodes. GDE and CCM had a similar high-frequency resistance (HFR) at 1.8 Ω cm², whereas GDE-CCM at twice as high ohmic resistance of 3.6 Ω cm². *Operando* X-ray CT cells have higher contact resistances due to design limitations that one encounters designing these cells. However, we expect this resistance not to be affected by the electrode used within the PEFC. Here, the high resistance of the GDE-CCM electrode is due to the poor interface between the GDE and CCM. Due to this poor interfacial contact, the cell was not able to hold current densities at 100 mA/cm² and produce positive potentials and thus no data is shown here for a current density hold.

5.3. *Operando* X-ray CT. In this section, we compare visualization of interfacial morphology and water distribution for three types of electrodes. This analysis is specific to the catalyst material, and here the electrocatalyst is highly hydrophobic, as we have already seen from the *in situ* study. Therefore, the water distribution is dictated by the electrocatalyst wettability. Generally, for a hydrophobic electrocatalyst, water will be ejected into the larger voids that are present in the media, as these are the locations of low capillary pressure (according to the Young−Laplace equation). After these are filled, it will fill the smaller voids and only later mesopores. Figure 6 shows *operando* cross-section tomographs for the GDE configuration of the PEFC. Compared to previous studies,[28,30] the GDE thickness here is reduced to <100 μm by optimizing the drying process. As a result of the synthesis
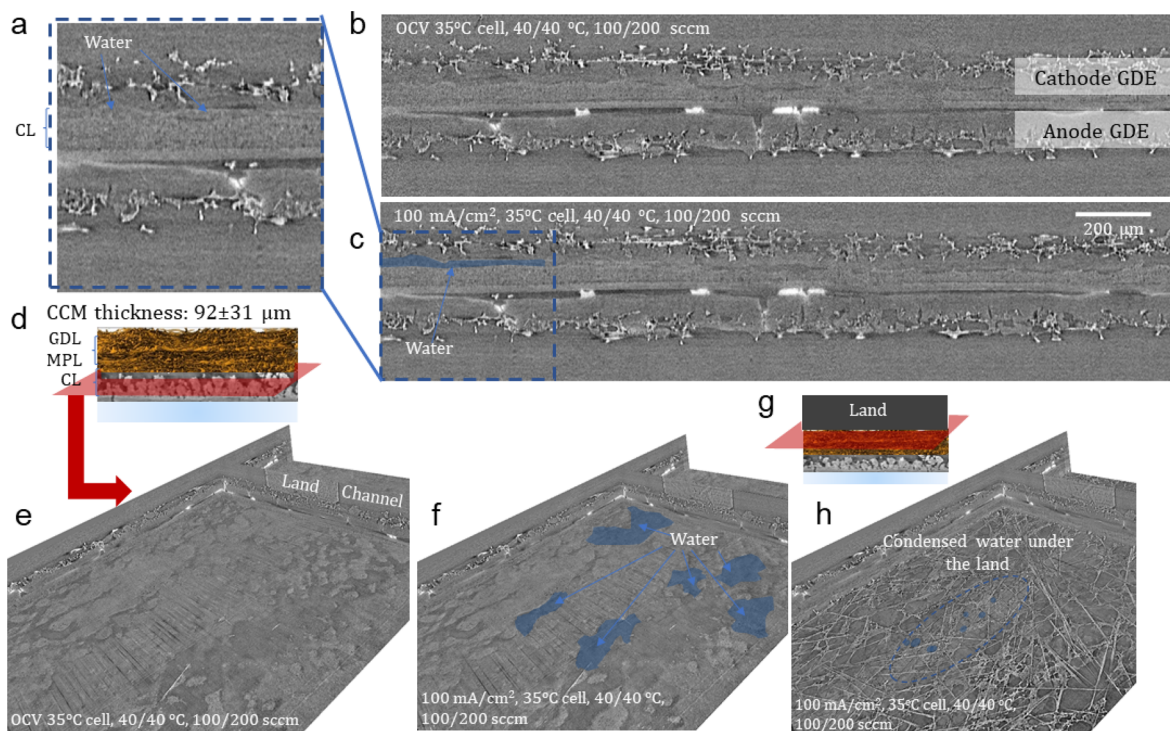
Figure 7. *Operando* X-ray CT cross sections for the cell with the CCM. The comparison of the cross sections under the channel (with part (a) the zoom-in) between the cell operating at (b) OCV and (c)100 mA/cm². In-plane view (with part (d) the location) of the CL|PEM interface at (e) OCV and (f) 100 mA/cm². In-plane view (with part (g) the location) at the GDL|land interface at (h) 100 mA/cm². Selected locations of interfacial water accumulation are shown with false coloring.
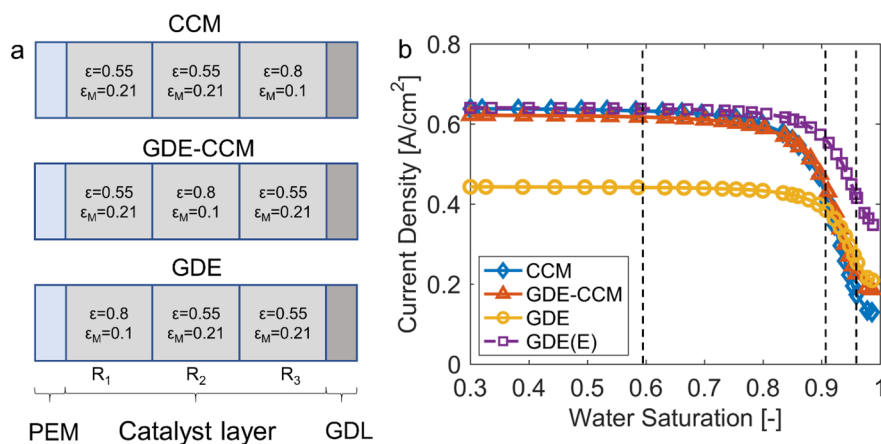

Figure 8. (a) Schematic of modeling domains and properties for the catalyst layer in the CCM, GDE-CCM, and GDE configurations. The regions R1, R2, and R3 are also labeled within the CL. (b) Current density as a function of water saturation for CCM, GDE-CCM, GDE, and GDE(E) at 0.3 V and 40 °C. The dashed lines indicate the locations at which the spatial distributions were plotted.

process, the electrocatalyst is highly porous. Since the catalyst layer was deposited onto the MPL, its interface with the MPL is very smooth and fills some of the larger MPL cracks (i.e., no cracks were observed on the cathode side of the MPL). On the other hand, the interface with the membrane is rough, as the electrode evaporative drying is still not as uniform to result in a perfectly flat layer. As can be seen from Figure 6a, the anode MPL has large cracks and the bright layer is Pt electrocatalyst dispersed on carbon. The X-ray CT at OCV conditions (Figure 6b,e) is compared to that for 100 mA/cm² current density and 35 °C, overhumidified conditions (Figure 6c,f). Liquid water is seen to fill the large voids between the GDE and membrane, similar to what we observed before[28] and what

is dictated by our *in situ* study. Liquid water was not observed in the GDL indicating that the breakthrough pressure has not been reached and most of the water was residing at the GDE interface with the membrane. The in-plane view clearly shows connected large water clusters at this interface (Figure 6f).

Figure 7 shows X-ray CT data comparing OCV and 100 mA/cm² operation for the cell containing CCM. The thickness of the CCM was larger than the GDE, although we aimed for the same loading. Since the catalyst was deposited onto the membrane, its interface with membrane is very conformal. Furthermore, we do not observe any cracks within the catalyst layer, and the layer is overall more uniform compared to the GDE. This might be due to the catalyst drying behavior on
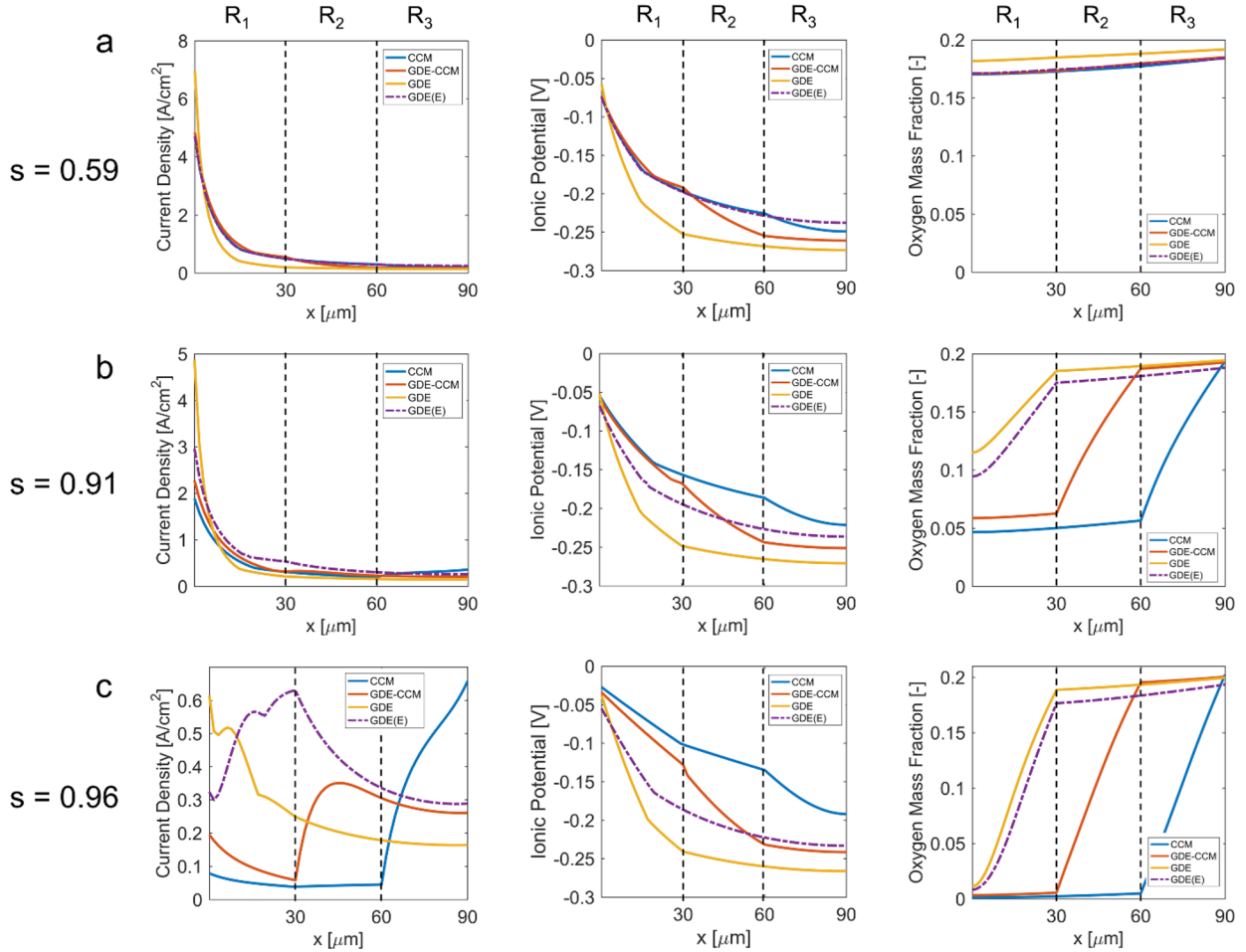
Figure 9. Spatial distributions of current density, ionic potential and oxygen mass fractions for the CCM GDE-CCM, GDE, and GDE(E) for three levels of saturation: (a) 0.59, (b) 0.91, and (c) 0.96. The regions of R1, R2, and R3 are marked too.

MPL vs Nafion, as shown by Fournier et al., with the substrate significantly influencing the final morphology of the film.[50] The catalyst layer still has a porous structure, but it is not as porous as in the GDE configuration. In this scenario, some of the voids are observed between the CCM and MPL. Comparing cross-sectional tomographs at OCV (Figure 7b,e) and 100 mA/cm² (Figure 7c,f), we observe the formation of a water film in these voids. Since the catalyst layer is hydrophobic, it is logical that liquid water will be ejected into the larger void regions. The water clusters that we see are not as large or continuous as in the case of GDE. For the same current density, the amount of water produced should be the same between the two cases. The remainder of water we observe is in the locations under the land (Figure 7h). Water at the interface between CCM and MPL can transport through MPL cracks and into the locations of the GDL under the land, as MPL cracks are the regions of low water transport resistance pathways.

Figure S4 shows the morphology of the GDE-CCM electrode, with thickness of 95 μm. We observe rough interface between CCM and GDE, and this rough interface can explain the high HFR observed electrochemically. For this scenario we could not hold the 100 mA/cm² sufficiently long to achieve steady-state, and therefore only two cross sections during preliminary run are shown here. Due to high resistance the potentials were crossing negative values and for this reason we could not operate the cell sufficiently to achieve a tomography scan.

5.4. Modeling Study. To generalize the findings from the X-ray CT *operando* observations, we utilize modeling framework with the three types of interfaces described in the experiments. Section 4 provides the model description and parameters, and Figure 8a shows the modeling domains porosity, ϵ, and volume fraction of ionomer ϵ_M for the cases of GDE, CCM, and GDE-CCM. Essentially, the catalyst layer is divided into three subdomains, R1, R2, and R3. The domain that forms the interface of interest (R3 for the CCM, R1 for the GDE, and R2 for the GDE-CCM) has increased porosity (due to its rough nature) of 0.8 and reduced ionomer content of 0.1, as the ionomer volume fraction depends on the solid fraction. We also created a hypothetical enhanced GDE that has the same volume fraction of ionomer in the interfacial subsection as in the others and termed it as GDE(E). In practice, it is possible to add a dilute Nafion layer between membrane and GDE to improve its adhesion.[36] The motivation to create this idealized configuration is to understand how well the GDE can perform, when not subject to ionic transport limitations.

As shown in Figure 8b, the current density is a function of average liquid water saturation in the catalyst layer for all three types of electrodes. For a range of saturation values (0.3−0.8), the current density remains constant, indicating that the catalyst layer has a large water capacity. For the CCM, GDE-CCM, and GDE(E), the current density is at 0.62 A/cm², whereas for GDE it is lower at 0.45 A/cm². Below, we will look

into the through-plane distributions for all four cases, but it is apparent that the ionic conductivity is a limiting factor for this GDE. When liquid water saturation crosses a certain threshold value, flooding occurs and current densities decrease with increasing saturation. This saturation threshold value is larger for the GDE of about 0.9 compared to the CCM and GDE CCM of about 0.85.

We choose three saturation levels, which are indicated by black dashed lines in Figure 8b for a detailed analysis. These three saturations correspond to current densities of (1) plateau regime, (2) transitional region, and (3) flooded region. Figure 9 shows spatial distributions within the catalyst layer for current density, ionic potential, and oxygen mass fraction. For the first scenario, the liquid water saturation is low and oxygen transport is not blocked. For all the catalyst layers, the oxygen mass fraction does not change much through the thickness of the CL as shown in Figure 9a. Local current density peaks in the R1 domain for all the catalyst layers and decreases with the x distance away from the membrane. Due to high local volumetric current densities, the CL becomes limited by the ohmic losses and we observe significant proton transport limitations, as ionic potential decreases from -0.05 V to -0.25 V through the 90 μm of CL thickness. The CCM has the highest volume fraction of ionomer next to the membrane resulting in higher ionic potential. The GDE has the lowest volume fraction of the ionomer in R1, resulting in a large decrease of ionic potential. This decrease also explains its lower current densities compared to the other types of catalyst layers. The CCM and GDE-CCM has the same volume fraction in R1, and they have a similar ionic potential as shown in Figure 9a. Then in R2, the ionic potential of GDE-CCM decreases faster comparied to CCM due to a lower volume fraction of ionomer.

For the second scenario of a transitional region, the saturation is 0.91 and most of the pores within the catalyst layers are filled by liquid water (progressing from larger to smaller for the hydrophobic electrocatalyst) and the impact of oxygen transport becomes important. The interfacial regions of R1, R2, and R3 are flooded in the GDEs, GDE-CCM, CCM, respectively. Oxygen concentration decreases dramatically through the flooded regions. For the CCM, the region with the largest voids is next to the MPL and flooding this layer blocks oxygen delivery to the whole catalyst layer. As a result, CCM has the lowest overall oxygen concentration, though it still has the highest ionic potential. GDE has the highest overall oxygen concentration but still with the lowest ionic potential. GDE-CCM has the R2 region flooded, which cuts off R1 region from oxygen delivery but still has R2 and R3 regions as active. The GDE(E) has improved ionic conductivity and high oxygen delivery, hence it has the largest current density. From the other three layers, the GDE-CCM, which has a compromise of ionic and oxygen concentrations, has the second highest current density. Interestingly, most of the current is still focused next to the membrane, indicating that even at these reduced current densities, ionic conductivity is still a limiting factor.

When the saturation is 0.96, almost all the voids within the catalyst layer are filled with liquid water. Oxygen transport becomes the most important limiting factor, as current densities are no longer concentrated next to the membrane. The oxygen concentration trend is similar to the previous case, but the decrease is more pronounced. The GDE(E) has the highest current density with the peak in the R1, as ionic

conductivity is still high there. The GDE has the second highest current density, peaking in R1, as the ionic potential is the highest there. As we can see in Figure 9c, the oxygen mass fraction is near zero after the flooded region. For the CCM case, we observe the shift in current density into the R3 region, as the reaction becomes oxygen limited. In R2, GDE-CCM has the highest local current density due to the relatively good ionic potential and oxygen concentration. Comparing the second column in Figure 9, we can see that the shape of the ionic potential curves is almost independent of saturation. This is because ion transport is assumed only in the ionomer phase and ion transport in liquid water is not considered in this model. At lower saturations, the oxygen concentration is higher, which results in a higher ORR rate.

To summarize, when flooding occurs it is desirable to have a good contact between the catalyst layer and MPL to ensure that there is no water pooling in these locations. The CCM configuration is not ideal, as in the case of imperfect contact with MPL, water will accumulate at the interface as observed in the X-ray CT data, observed in polarization curves at low temperatures, and confirmed by modeling. GDE-CCM alleviates the problem as water pooling occurs at the interface within the catalyst layer, cutting off only half of the catalyst layer in the scenario of severe flooding. The GDE seems to be the best type of layer, but one has to be careful to ensure good ionic contact between the catalyst layer and membrane or else the reaction will be ohmicly limited as suggested by the modeling study.

6. CONCLUSIONS

In this paper, three types of PGM-free electrodes, CCM, GDE-CCM, and GDE, were fabricated and their performance was analyzed within the operating PEFC. The results show that the through-thickness inhomogeneity introduced by the evaporative drying process plays a critical role in water management and cell performance. As a result of the deposition process, an interfacial region exists within these electrodes that has larger porosity and significant surface roughness. This porous region locates at the CL|MPL interface, middle of the CL and CL| PEM interface for the CCM, GDE-CCM, and GDE, respectively. An *in situ* X-ray CT study has been conducted, where water is injected into the PGM-free GDE at three liquid pressures of 1.5, 5, and 10 mbar and its distribution and catalyst wetting properties are observed. The electrocatalyst showed to be highly hydrophobic, with water wetting only larger macropores even at a high liquid pressure of 10 mbar.

The *operando* X-ray CT study shows that water pooling is observed at the CL|PEM interface for the GDE case and the CL|MPL interface for the CCM case for 100 mA/cm^2 current density and 35 °C temperature at overhumidified gas feeds. The reason for water pooling in these locations is that these are where the larger voids are present, and due to the hydrophobic nature of the catalyst, water is ejected into these larger voids. For the GDE-CCM electrode, no conclusive answer was provided for water distribution because the interface was rough, resulting in significant ohmic loss. Experimentally measured polarization curves show that out of the three cells, the GDE-CCM has the best performances at 45 and 35 °C. At these low temperatures, the CCM showed half the current density at a low applied potential compared to the GDE and GDE-CCM cases.

The computational model supplemented the experimental results. The model has shown that the current density is a

function of liquid water saturation, and at 0.3 V and 40 °C three regimes were observed: (1) a plateau at relatively low saturations, (2) a transitional region at high saturation, where current density starts decreasing, and (3) a flooded region. At low saturations, the current density is independent of saturation since oxygen diffusion is not inhibited by liquid water and oxygen concentration is not the limiting factor. After some critical point, water flooding blocks oxygen diffusion and current density decreases with saturation due to depletion of oxygen. The cases of the three types of electrodes and additional enhanced GDE (GDE(E)) at three saturation levels, 0.59, 0.91, and 0.96 were studied in detail. At low saturation (0.59), oxygen concentration is high in the whole catalyst layer, whereas the ionic potential is the limiting factor. The CCM with the highest ionomer volume fraction next to the PEM side has the highest current density among the three electrodes. At intermediate saturation (0.91), water flooding starts to influence the cell performance. Both oxygen concentration and ionic potential have a significant impact on the current density. In this scenario, GDE-CCM has the highest current density among the three electrodes. This is because in the GDE-CCM configuration, both ion and oxygen accessibilities are sufficient for this saturation, whereas CCM becomes oxygen-transport limited and GDE remains ion-transport limited. At high saturation (0.96), the interfacial region within these electrodes severely blocks gas diffusion due to water flooding. GDE with this interfacial porous region on the PEM side enables the highest overall oxygen concentration in the catalyst layer and it has the highest current density. CCM becomes even more oxygen-transport limited, and GDE-CCM also shows oxygen-transport limitations. The major issue with the GDE is that the low volume fraction of ionomer in the interfacial porous region hinders ion conduction. This can be improved by coating the layer or PEM with a dilute Nafion ionomer to improve layer adhesion to the PEM. The GDE(E), which is an enhanced GDE without the ion transport limitation, shows the highest current density at all saturations.

The model study supports the X-ray CT data by showing that at low temperatures, the interfacial porous regions flood and limit PGM-free PEFC performance. Furthermore, it explains the polarization curves collected that show the CCM lower current densities at low temperatures. The model predicts water pooling and oxygen transport limitations for the CCM-type electrodes. A more-controlled evaporative drying fabrication method is needed to ensure conformal interfaces between the electrode and PEM and also MPL.

■ AUTHOR INFORMATION

Corresponding Author
*E-mail: Iryna.Zenyuk@uci.edu.
ORCID ©
Dilworth Y. Parkinson: 0000-0002-1817-0716
Plamen Atanassov: 0000-0003-2996-472X
Iryna V. Zenyuk: 0000-0002-1612-0475
Notes
The authors declare no competing financial interest.

■ ACKNOWLEDGMENTS

■ REFERENCES

(1) Debe, M. K. Electrocatalyst Approaches and Challenges for Automotive Fuel Cells. *Nature* **2012**, *486*, 43.

(2) Sinha, J. *Cost Analyses of Fuel Cell Stacks/Systems,*https://hydrogendoedev.nrel.gov/pdfs/progress10/v_a_3_sinha.pdf

(3) Saha, M. S.; Gullá, A. F.; Allen, R. J.; Mukerjee, S. High Performance Polymer Electrolyte Fuel Cells with Ultra-Low Pt Loading Electrodes Prepared by Dual Ion-Beam Assisted Deposition. *Electrochim. Acta* **2006**, *51*, 4680−4692.

(4) Kongkanand, A.; Mathias, M. F. The Priority and Challenge of High-Power Performance of Low-Platinum Proton-Exchange Membrane Fuel Cells. *J. Phys. Chem. Lett.* **2016**, *7*, 1127−1137.

(5) Gasteiger, H. A.; Kocha, S. S.; Sompalli, B.; Wagner, F. T. Activity Benchmarks and Requirements for Pt, Pt-Alloy, and Non-Pt Oxygen Reduction Catalysts for Pemfcs. *Appl. Catal., B* **2005**, *56*, 9−35.

(6) Artyushkova, K.; Serov, A.; Rojas-Carbonell, S.; Atanassov, P. Chemistry of Multitudinous Active Sites for Oxygen Reduction Reaction in Transition Metal−Nitrogen−Carbon Electrocatalysts. *J. Phys. Chem. C* **2015**, *119*, 25917−25928.

(7) Chen, Y.; Matanovic, I.; Weiler, E.; Atanassov, P.; Artyushkova, K. Mechanism of Oxygen Reduction Reaction on Transition Metal−Nitrogen−Carbon Catalysts: Establishing the Role of Nitrogen-Containing Active Sites. *ACS Applied Energy Materials* **2018**, *1*, 5948−5953.

(8) Shao, M.; Chang, Q.; Dodelet, J.-P.; Chenitz, R. Recent Advances in Electrocatalysts for Oxygen Reduction Reaction. *Chem. Rev.* **2016**, *116*, 3594−3657.

(9) Serov, A.; Artyushkova, K.; Atanassov, P. Fe-N-C Oxygen Reduction Fuel Cell Catalyst Derived from Carbendazim: Synthesis, Structure, and Reactivity. *Adv. Energy Mater.* **2014**, *4*, 1301735.

(10) Dai, L.; Xue, Y.; Qu, L.; Choi, H.-J.; Baek, J.-B. Metal-Free Catalysts for Oxygen Reduction Reaction. *Chem. Rev.* **2015**, *115*, 4823−4892.

(11) Zhu, C.; Li, H.; Fu, S.; Du, D.; Lin, Y. Highly Efficient Nonprecious Metal Catalysts Towards Oxygen Reduction Reaction Based on Three-Dimensional Porous Carbon Nanostructures. *Chem. Soc. Rev.* **2016**, *45*, 517−531.

(12) Nie, Y.; Li, L.; Wei, Z. Recent Advancements in Pt and Pt-Free Catalysts for Oxygen Reduction Reaction. *Chem. Soc. Rev.* **2015**, *44*, 2168−2201.

(13) Chung, H. T.; Won, J. H.; Zelenay, P. Active and Stable Carbon Nanotube/Nanoparticle Composite Electrocatalyst for Oxygen Reduction. *Nat. Commun.* **2013**, *4*, 1922.

(14) Wu, G.; More, K. L.; Johnston, C. M.; Zelenay, P. High-Performance Electrocatalysts for Oxygen Reduction Derived from Polyaniline, Iron, and Cobalt. *Science* **2011**, *332*, 443−447.

(15) Lefèvre, M.; Proietti, E.; Jaouen, F.; Dodelet, J.-P. Iron-Based Catalysts with Improved Oxygen Reduction Activity in Polymer Electrolyte Fuel Cells. *Science* **2009**, *324*, 71−74.

(16) Proietti, E.; Jaouen, F.; Lefèvre, M.; Larouche, N.; Tian, J.; Herranz, J.; Dodelet, J.-P. Iron-Based Cathode Catalyst with Enhanced Power Density in Polymer Electrolyte Membrane Fuel Cells. *Nat. Commun.* **2011**, *2*, 416.

(17) Deng, D.; Yu, L.; Chen, X.; Wang, G.; Jin, L.; Pan, X.; Deng, J.; Sun, G.; Bao, X. Iron Encapsulated within Pod-Like Carbon Nanotubes for Oxygen Reduction Reaction. *Angew. Chem., Int. Ed.* **2013**, *52*, 371−375.

(18) Jaouen, F.; Charreteur, F.; Dodelet, J. P. Fe-Based Catalysts for Oxygen Reduction in Pemfcs: Importance of the Disordered Phase of the Carbon Support. *J. Electrochem. Soc.* **2006**, *153*, A689−A698.

(19) Jaouen, F.; Proietti, E.; Lefèvre, M.; Chenitz, R.; Dodelet, J.-P.; Wu, G.; Chung, H. T.; Johnston, C. M.; Zelenay, P. Recent Advances in Non-Precious Metal Catalysis for Oxygen-Reduction Reaction in Polymer Electrolyte Fuel Cells. *Energy Environ. Sci.* **2011**, *4*, 114−130.

(20) Kramm, U. I.; et al. Structure of the Catalytic Sites in Fe/N/C-Catalysts for O2-Reduction in Pem Fuel Cells. *Phys. Chem. Chem. Phys.* **2012**, *14*, 11673−11688.

(21) Qu, L.; Liu, Y.; Baek, J.-B.; Dai, L. Nitrogen-Doped Graphene as Efficient Metal-Free Electrocatalyst for Oxygen Reduction in Fuel Cells. *ACS Nano* **2010**, *4*, 1321−1326.

(22) Tylus, U.; Jia, Q.; Strickland, K.; Ramaswamy, N.; Serov, A.; Atanassov, P.; Mukerjee, S. Elucidating Oxygen Reduction Active Sites in Pyrolyzed Metal−Nitrogen Coordinated Non-Precious-Metal Electrocatalyst Systems. *J. Phys. Chem. C* **2014**, *118*, 8999−9008.

(23) Martinez, U.; Komini Babu, S.; Holby, E. F.; Zelenay, P. Durability Challenges and Perspective in the Development of Pgm-Free Electrocatalysts for the Oxygen Reduction Reaction. *Current Opinion in Electrochemistry* **2018**, *9*, 224−232.

(24) Leonard, N. D.; Artyushkova, K.; Halevi, B.; Serov, A.; Atanassov, P.; Barton, S. C. Modeling of Low-Temperature Fuel Cell Electrodes Using Non-Precious Metal Catalysts. *J. Electrochem. Soc.* **2015**, *162*, F1253−F1261.

(25) Lopes, T.; Kucernak, A.; Malko, D.; Ticianelli, E. A. Mechanistic Insights into the Oxygen Reduction Reaction on Metal−N−C Electrocatalysts under Fuel Cell Conditions. *ChemElectroChem* **2016**, *3*, 1580−1590.

(26) Babu, S. K.; Chung, H.; Zelenay, P.; Litster, S. Modeling Electrochemical Performance of the Hierarchical Morphology of Precious Group Metal-Free Cathode for Polymer Electrolyte Fuel Cell. *J. Electrochem. Soc.* **2017**, *164*, F1037−F1049.

(27) Komini Babu, S.; Chung, H. T.; Zelenay, P.; Litster, S. Resolving Electrode Morphology's Impact on Platinum Group Metal-Free Cathode Performance Using Nano-Ct of 3d Hierarchical Pore and Ionomer Distribution. *ACS Appl. Mater. Interfaces* **2016**, *8*, 32764−32777.

(28) Normile, S. J.; Sabarirajan, D. C.; Calzada, O.; De Andrade, V.; Xiao, X.; Mandal, P.; Parkinson, D. Y.; Serov, A.; Atanassov, P.; Zenyuk, I. V. Direct Observations of Liquid Water Formation at Nano- and Micro-Scale in Platinum Group Metal-Free Electrodes by Operando X-Ray Computed Tomography. *Materials Today Energy* **2018**, *9*, 187−197.

(29) Pavlicek, R.; Barton, S. C.; Leonard, N.; Romero, H.; McKinney, S.; McCool, G.; Serov, A.; Abbott, D.; Atanassov, P.; Mukerjee, S. Resolving Challenges of Mass Transport in Non Pt-Group Metal Catalysts for Oxygen Reduction in Proton Exchange Membrane Fuel Cells. *J. Electrochem. Soc.* **2018**, *165*, F589−F596.

(30) Serov, A.; Shum, A. D.; Xiao, X.; De Andrade, V.; Artyushkova, K.; Zenyuk, I. V.; Atanassov, P. Nano-Structured Platinum Group Metal-Free Catalysts and Their Integration in Fuel Cell Electrode Architectures. *Appl. Catal., B* **2018**, *237*, 1139.

(31) Stariha, S.; Artyushkova, K.; Workman, M. J.; Serov, A.; McKinney, S.; Halevi, B.; Atanassov, P. Pgm-Free Fe-N-C Catalysts for Oxygen Reduction Reaction: Catalyst Layer Design. *J. Power Sources* **2016**, *326*, 43−49.

(32) Reshetenko, T. V.; St-Pierre, J. Separation Method for Oxygen Mass Transport Coefficient in Gas and Ionomer Phases in Pemfc Gde. *J. Electrochem. Soc.* **2014**, *161*, F1089−F1100.

(33) Serov, A.; Shum, A. D.; Xiao, X.; De Andrade, V.; Artyushkova, K.; Zenyuk, I. V.; Atanassov, P. Nano-Structured Platinum Group Metal-Free Catalysts and Their Integration in Fuel Cell Electrode Architectures. *Appl. Catal., B* **2018**, *237*, 1139−1147.

(34) Kabir, S.; Lemire, K.; Artyushkova, K.; Roy, A.; Odgaard, M.; Schlueter, D.; Oshchepkov, A.; Bonnefont, A.; Savinova, E.; Sabarirajan, D. C. Platinum Group Metal-Free Nimo Hydrogen Oxidation Catalysts: High Performance and Durability in Alkaline Exchange Membrane Fuel Cells. *J. Mater. Chem. A* **2017**, *5*, 24433−24443.

(35) Kim, G.; Eom, K.; Kim, M.; Yoo, S. J.; Jang, J. H.; Kim, H.-J.; Cho, E. Design of an Advanced Membrane Electrode Assembly Employing a Double-Layered Cathode for a Pem Fuel Cell. *ACS Appl. Mater. Interfaces* **2015**, *7*, 27581−27585.

(36) Shahgaldi, S.; Alaefour, I.; Li, X. Impact of Manufacturing Processes on Proton Exchange Membrane Fuel Cell Performance. *Appl. Energy* **2018**, *225*, 1022−1032.

(37) Zenyuk, I. V. Bridging X-Ray Computed Tomography and Computational Modeling for Electrochemical Energy-Conversion and − Storage. *Current Opinion in Electrochemistry* **2019**, *13*, 78−85.

(38) Komini Babu, S.; Chung, H. T.; Zelenay, P.; Litster, S. Resolving Electrode Morphology's Impact on Platinum Group Metal-Free Cathode Performance Using Nano-Ct of 3d Hierarchical Pore and Ionomer Distribution. *ACS Appl. Mater. Interfaces* **2016**, *8*, 32764−32777.

(39) Arif, M.; Hussey, D. S.; Baltic, E. M.; Jacobson, D. L. Neutron Imaging Facility Development and Research Trend at Nist. *Phys. Procedia* **2015**, *69*, 210−217.

(40) Zenyuk, I. V.; Lambirac, A.; Eller, J.; Parkinson, D. Y.; Marone, F.; Büchi, F. N.; Weber, A. Z. Investigating Evaporation in Gas Diffusion Layers for Fuel Cells with X-Ray Computed Tomography. *J. Phys. Chem. C* **2016**, *120*, 28701−28711.

(41) Balliet, R. J. *Modeling Cold Start in a Polymer-Electrolyte Fuel Cell.* Ph.D. Thesis, University of California, Berkeley, CA, 2010.

(42) Balliet, R. J.; Newman, J. Cold Start of a Polymer-Electrolyte Fuel Cell I. Development of a Two-Dimensional Model. *J. Electrochem. Soc.* **2011**, *158*, B927−B938.

(43) Zenyuk, I. V.; Das, P. K.; Weber, A. Z. Understanding Impacts of Catalyst-Layer Thickness on Fuel-Cell Performance Via Mathematical Modeling. *J. Electrochem. Soc.* **2016**, *163*, F691−F703.

(44) Zenyuk, I. V.; Parkinson, D. Y.; Connolly, L. G.; Weber, A. Z. Gas-Diffusion-Layer Structural Properties under Compression Via X-Ray Tomography. *J. Power Sources* **2016**, *328*, 364−376.

(45) Spernjak, D.; Mukundan, R.; Borup, R. L.; Connolly, L. G.; Zackin, B. I.; De Andrade, V.; Wojcik, M.; Parkinson, D. Y.; Jacobson, D. L.; Hussey, D. S.; More, K. L.; Chan, Th.; Weber, A. Z.; Zenyuk, I. V. Enhanced Water Management of Polymer Electrolyte Fuel Cells with Novel Microporous Layers. *ACS Applied Energy Materials* **2018**, *1*, 6006.

(46) Bird, R. B.; Lightfoot, E. N.; Stewart, W. E. *Transport Phenomena*; Wiley, 2002.

(47) Weber, A. Z.; Newman, J. Transport in Polymer-Electrolyte Membranes: Ii. Mathematical Model. *J. Electrochem. Soc.* **2004**, *151*, A311−A325.

(48) Weber, A. Z. Gas-Crossover and Membrane-Pinhole Effects in Polymer-Electrolyte Fuel Cells. *J. Electrochem. Soc.* **2008**, *155*, B521−B531.

(49) Zenyuk, I. V.; Parkinson, D. Y.; Hwang, G.; Weber, A. Z. Probing Water Distribution in Compressed Fuel-Cell Gas-Diffusion Layers Using X-Ray Computed Tomography. *Electrochem. Commun.* **2015**, *53*, 24−28.

(50) Fournier, R.; Shum, A. D.; Liu, J.; Sabarirajan, D. C.; Xiao, X.; Zenyuk, I. V. Combined Infrared Thermography, X-Ray Radiography, and Computed Tomography for Ink Drying Studies. *ACS Applied Energy Materials* **2018**, *1*, 6101−6114.